Reversibility of metal-hydride anodes in all-solid-state lithium secondary battery operating at room temperature

A. El kharbachi[a,*], Y. Hu[b], M.H. Sørby[a], J.P. Mæhlen[a], P.E. Vullum[c], H. Fjellvåg[b], B.C. Hauback[a]

[a] Institute for Energy Technology, P.O. Box 40, NO-2027 Kjeller, Norway
[b] Centre for Materials Science and Nanotechnology, University of Oslo, P.O. Box 1126, Blindern, NO-0318 Oslo, Norway
[c] SINTEF Materials and Chemistry, P.O. Box 4760 Sluppen, NO-7465 Trondheim, Norway

Abstract

The impact on the performance of conversion-type MgH_2 anodes by using solid state electrolyte is reported. MgH_2 anodes (~26 µm thick) made from homogenous slurries and subsequent drying, are used as model systems along with $Li(BH_4)_{0.75}I_{0.25}–0.8Li_2S\cdot0.2P_2S_5$ as solid electrolyte in an "all-solid-state room-temperature secondary battery". Electrochemical tests are carried out to investigate cycling properties and elucidate reversibility aspects during the conversion reaction. A major enhancement in performance is observed for the all-solid-state battery compared to MgH_2 anodes using carbonate-based liquid electrolytes. This shows that good compatibility and improved reversibility can be obtained for hydride anodes when associated with borohydride-based electrolyte in a Li-ion cell operating at room temperature.

Keywords: MgH_2-based anode, reversibility, conversion reaction, solid electrolyte, Li-ion battery

1   Introduction

Conversion-type anodes are interesting for Li-ion batteries owing to their specific mechanistic properties and high capacity compared to conventional insertion-type anodes such as graphite. Hydride based anodes, for example MgH_2, have been demonstrated for Li-ion batteries [1,2]. MgH_2 reacts with 2Li in a chemical reaction (redox potential 0.45 V *vs.* Li^+/Li), leading to the formation of 2LiH and Mg and thus allowing a storage capacity of about 2 Ah g^{-1} with low polarization during the discharge-charge processes [1,3,4]. Besides, these materials have the peculiarity to cover the weaknesses of oxide based conversion-type anodes in which the high working potential and large (de)lithiation cycling hysteresis hinder its quick application in Li-ion batteries [5]. On the other hand, the application of hydride anodes is still a challenge owing to capacity loss after several cycles, starting either from the charged or discharged states [2,3]. The bulk volume variation between these two states, i.e. *tetra*-MgH_2 and 2LiH/Mg, is about 83% which can influence the electron conductivity between the particles [6]. The reported electrochemical tests using MgH_2 show only a partial reversibility at room temperature (*RT*), either using liquid or solid electrolytes [1,3,7-9]. A reversible capacity of ca. 75% is reached for a liquid electrolyte during the first cycle [2,3,6]. However, in solid state using the glass system Li_2S-P_2S_5, Ikeda *et al.*[7] reported around 31% reversible capacity at *RT*. Possible interaction with the solid electrolyte (SE) at the electrode/electrolyte interface was pointed out. Better performance has been reached using $LiBH_4$ as SE at higher temperatures at 120°C [10-12],

or Li(BH$_4$)$_{0.75}$I$_{0.25}$ at 150°C [13]. Considering formulation effects (morphology, additives and coating) which may influence the cycling performance [14-17], an optimization of the design of the electrode is required before any cell with a suitable choice of SE can be made.

Here, we report our recent findings on the reversibility of MgH$_2$ anodes at *RT* when embedded in a SE for tests in a Li-ion cell configuration. A new electrolyte with reasonable ionic conductivities has been synthesized; Li$_2$S-P$_2$S$_5$ is stabilized by adding Li(BH$_4$)$_{0.75}$I$_{0.25}$ followed by annealing. The presence of SE at *RT* removes most issues connected with SEI-like degradations, even though some other interfacial aspects appear according to the existence of path dependence in this electrode. The obtained experimental results are presented and discussed in relation to previous analytical works [16].

2   Experimental

MgH$_2$ was purchased from Alpha-Aesar (98% purity). The MgH$_2$ powders were ball-milled (24h) under hydrogen atmosphere (5 MPa) using planetary ball-mill with stainless steel vials and balls (ball-to-powder ratio 40:1, 400 rpm). LiBH$_4$ (95%), LiI (99.9%), Li$_2$S (99.98%) and P$_2$S$_5$ (99%) were purchased from Sigma-Aldrich. The halide-stabilized hexagonal phase Li(BH$_4$)$_{0.75}$I$_{0.25}$ was synthesized according to the procedure described by Miyazaki *et al.*[18]. The amorphous precursor 0.8Li$_2$S·0.2P$_2$S$_5$ was prepared by ball-milling for 20h using planetary ball-mill (ball-to-powder ratio

40:1, 370 rpm) [19,20].

Synchrotron radiation powder X-ray diffraction (SR-PXD) patterns were obtained at the Swiss-Norwegian Beamlines (SNBL, BM01), ESRF, Grenoble with a Pilatus2M 2-dimensional detector and a wavelength of 0.77787 or 0.6973 Å. The samples were contained in 0.5 mm borosilicate capillaries that were rotated 90° during 30 second exposure. The sample - detector distance was 345.97 mm. 1D data were obtained by integration of the 2D diffraction patterns using the program Bubble [21]. Crystallite sizes were determined with the Scherrer equation from the FWHM (Full Width at Half Maximum) of the diffraction peaks, corrected for instrumental broadening using LaB_6 as standard. The microstrain contribution to the broadening was disregarded as it remains at a minimum level after long-time milling [22]. TEM was performed with a double Cs corrected JEOL coldFEG ARM200CF, operated at 200 kV. Focused ion beam – scanning electron microsocopy (FIB-SEM) was carried out with a FEI Helios 600 dualBeam FIB. The Ga^+ ion beam was used to cut down through the electrode for cross-section imaging.

The ionic conductivity of the solid electrolytes was investigated by Electrochemical Impedance Spectroscopy (EIS) measurements using a Novocontrol Alpha-A frequency analyzer (Montabaur, Germany). The as-milled materials were first pressed into pellets with a diameter of 8 mm and thicknesses from 0.6 to 0.9 mm by using a uniaxial press at around 550 MPa. The pellets were sandwiched between lithium foils as non-blocking electrodes, and sealed in a stainless steel cell.

Temperature-dependent measurements were performed in Ar using a Probostat (NorECs AS) sample holder from RT up to 120°C. Measured impedance spectra were analyzed by equivalent circuits using ZView2 software (Scribner Associates Inc.). Total conductivity was calculated using the resistance obtained from data fitting and the sample geometry.

All-solid-state battery cells were prepared in coin cell configuration using standard TiS_2 and MgH_2 as active electrodes, respectively. For the cell with TiS_2, the TiS_2 (99.9%, Sigma-Aldrich) powders and the prepared SE powders were weighed in a 2:3 mass ratio and manually mixed by an agate mortar/pestle. The obtained mixture was used as the electrode composite. Less than 6 mg of this composite and 50 mg of the SE were introduced in a 10 mm die set and pressed together uniaxially at 240 MPa. A Li foil was placed on the opposite side of the material composite as counter/reference electrode. The resulted multi-layer pellet was inserted in a CR2032 coin cell. To ensure thinner electrodes and to better optimize the diffusion pathways, thin electrode tapes (26 µm) containing MgH_2 were prepared and adhered on the dendrite surface of the Cu foil [16]. The final electrodes were cold pressed with the SE and lithium foil at 240 MPa. The following cells were then assembled:

Battery 1: TiS_2/SE | SE | Li

Battery 2: MgH_2-tape | SE | Li

All handling was performed in a MBraun® glove box under Ar atmosphere (H_2O and O_2 < 0.1 ppm).

A home-made "ETH-cell" battery cell consisting of a stainless-steel outer casing and inner parts in

titanium was used for cycling. The cells were cycled at 30°C (0.01 mA cm^{-2}) between 1.6 – 2.7 V for

TiS$_2$ and 0.2 – 2 V for MgH$_2$, respectively, using an Arbin Battery cycler (Arbin Instruments$^®$). The

voltage cut-off at 0.2 V was applied to avoid formation of Mg-Li solid solutions at lower voltage

[1,6].

3   Results and Discussion

3.1   Materials characterization and properties

Microstructural characteristics (SR-PXD) of the MgH$_2$ powder, as seen in Fig. 1, indicate a well

crystalline *tetra*-MgH$_2$ with significant presence of elemental Mg. Subsequent milling leads to

reduced grain size (3-7 nm), given the broadening of the Bragg peaks. The microstrain is assumed to

be negligible and less than 0.1% [16]. The milled material shows no or very little presence of Mg,

presumably due to hydrogenation during the milling process. In accordance with previous works,

significant amounts of metastable *ortho*-MgH$_2$ is formed and depends on the milling conditions [16].

However, it is not clear whether the formation of *ortho*-MgH$_2$ occurs during hydrogenation of the

Mg impurity or results from a phase transition during the mechanical milling [23].
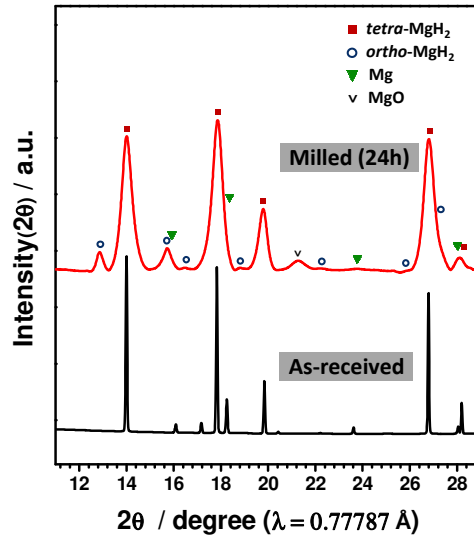
Figure 1. SR-PXD patterns of the 24h-milled MgH_2 under H_2 atmosphere 5 MPa.

Particles with sizes in the order of 150 nm can be seen in the TEM images (Fig. 2), though some larger agglomerates are still present. Zooming in on a selected single particle (bottom left), the image shows a square shaped morphology. Electron beam damage turns this 100 nm large crystal into a number of small facetted nanocrystal fragments with the same crystal structure. Continuous electron beam irradiation finally destroys the crystal (bottom right image in Fig. 2). The d-spacings calculated from the spots in the Fourier transform of the high resolution TEM image (inset) agree with $tetra$-MgH_2. Note that, milling for short times < 5h at the same conditions results in particles in the micron range (SEM, not shown).
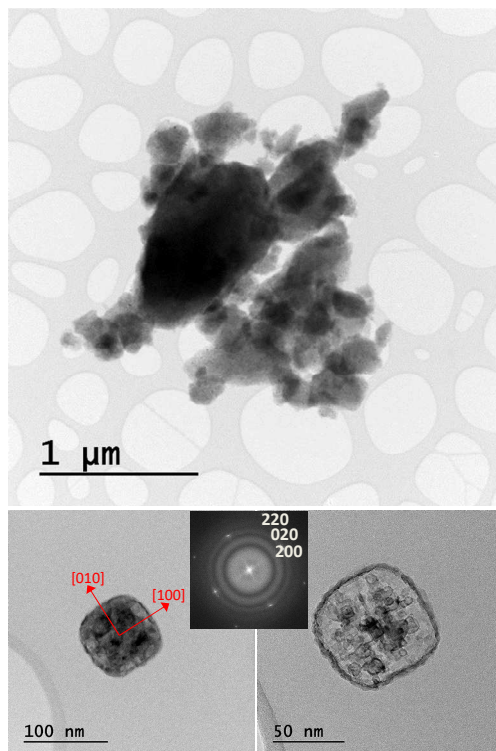
Figure 2. Bright field TEM micrographs of the 24h-milled MgH_2 under H_2 atmosphere 5 MPa: Overview picture (top) and higher magnification on one single particle (bottom). Inset: Fourier transform of the bright field TEM image.

With respect to SE, Fig. 3a shows the SR-PXD patterns of as-synthesized $Li(BH_4)_{0.75}I_{0.25}$ by the annealing method [18] and of $Li(BH_4)_{0.75}I_{0.25}$ milled with $0.8Li_2S \cdot 0.2P_2S_5$ system and after annealing at 240°C under 2 MPa H_2 pressure (final SE). In the milled mixture, the SR-PXD pattern indicates the presence of the $Li(BH_4)_{0.75}I_{0.25}$,Li_2S and P_2S_5. However, after annealing the peaks from $Li(BH_4)_{0.75}I_{0.25}$ and P_2S_5 are no longer visible while some excess of Li_2S still remains. The additional observed Bragg peaks could not be assigned to any phase(s) in the PDF-4 2016 database. Attempts to index the peaks do not result in any sensible suggested unit cell, thus indicating that more than one

new crystalline phase has formed. Fig. 3b displays the temperature dependent ionic conductivity of the Li(BH$_4$)$_{0.75}$I$_{0.25}$–0.8Li$_2$S·0.2P$_2$S$_5$ system before and after annealing. The as-milled sample exhibits a *RT* conductivity of around 1.5×10^{-5} S cm^{-1}, which increases gradually upon heating. Due to instability issues, probably due to the presence of unreacted P$_2$S$_5$, this measurement was limited to 80°C. The annealed sample (SE) shows more stable records of the impedance during the temperature ramp indicating improved thermal stability. The *RT* conductivity of SE is ~10^{-4} S cm^{-1}, about one order of magnitude higher than for the as-milled sample. Both conductivities follow an Arrhenius trend according to the relation: $\sigma T = \sigma_0 \exp(-E_a/kT)$. A lower activation energy of 0.37(1) eV is obtained for the annealed SE (Fig. 3b), indicating enhanced Li ions transport kinetics. Similar solid electrolytes based on the system LiBH$_4$-Li$_2$S-P$_2$S$_5$ have been reported with higher conductivities [24,25]. However, as the compositions are different, direct comparison with our electrolyte system containing iodine is not obvious.
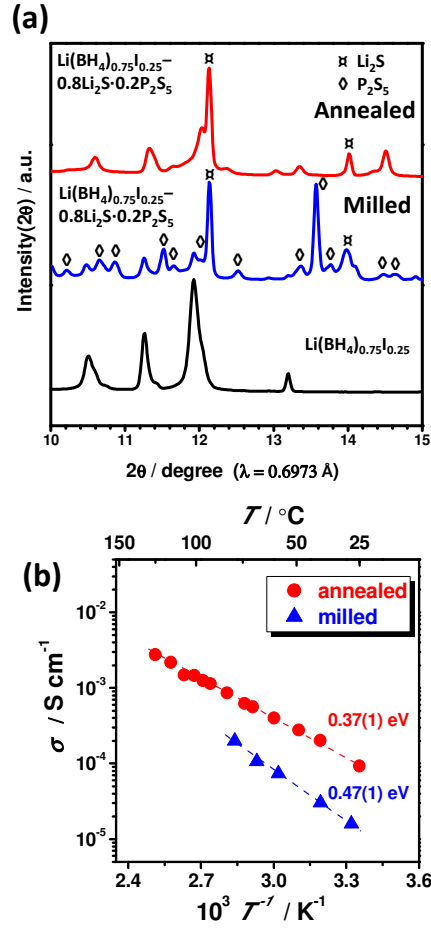
Figure 3. (a) SR-PXD patterns of synthesized $Li(BH_4)_{0.75}I_{0.25}$ before and after incorporation of the $0.8Li_2S \cdot 0.2P_2S_5$ system with subsequent milling and annealing. (b) Temperature-dependent ionic conductivities of the solid electrolyte $Li(BH_4)_{0.75}I_{0.25}-0.8Li_2S \cdot 0.2P_2S_5$. The data show the as-milled and annealed systems with derived activation energies. Standard deviations in parentheses.

3.2 Analysis and characterization of the assembled cells

3.2.1 Electrochemical tests

Cyclic voltammetry of the electrochemical cell Li│SE│Au has been performed (not shown), by

which the reversible stripping/platting of Li can be observed around 0 V with different scan rates. No

additional redox process is observed, suggesting an electrochemical window for this electrolyte up to

5 V *vs.* Li^{+}/Li. Battery tests are demonstrated by first using a standard TiS_2 electrode (theoretical

capacity 239 mAh g^{-1}), as reported on similar electrolyte systems such as $LiBH_4$, $Li(BH_4)_{0.75}I_{0.25}$ and

$90LiBH_4 \cdot 10P_2S_5$ [25-27]. Fig. 4a shows the good cyclability of this electrode at low applied currents.

Higher current densities were attempted but yielded poorer results. The capacity of the initial

discharge correspond to 89% of the theoretical capacity in agreement with the *RT* reported studies

with $77.5Li_2S \cdot 22.5P_2S_5$ electrolyte [28]. Up to one Li can be inserted assuming the complete

reaction : $xLi + TiS_2 \rightarrow Li_xTiS_2$. The sudden voltage drop/resumption at the initial discharge is

related to a solid-state reaction between the electrode and electrolyte. Such activation process to

create stable interface has been also reported in previous studies using $90LiBH_4 \cdot 10P_2S_5$ as solid

electrolyte [25]. The discharge/charge profiles of the three first cycles obtained with an MgH_2

electrode and annealed SE are shown in Fig. 4b. It presents flat discharge-charge plateaus and low

polarization-hysteresis. The electrochemical behavior of MgH_2 in liquid electrolyte is given in Fig.

4c for comparison using the same morphology electrodes as in Fig. 4b. Despite the observed high

capacity during discharge, the electrode in liquid electrolyte demonstrates lower reversibility yield

compared to when solid electrolyte is used. It can be noticed that the discharge plateau is slightly

lowered by 50 mV compared to the liquid electrolyte at slow rate, and thus leading to a slight

increase of the polarization. This factor can, however, be influenced by the electrode/Li distances

which may need to be optimized for the solid-state configuration. The obtained discharge capacity

reflects only a part of the total active material; probably the loaded mass is not fully involved in the process.
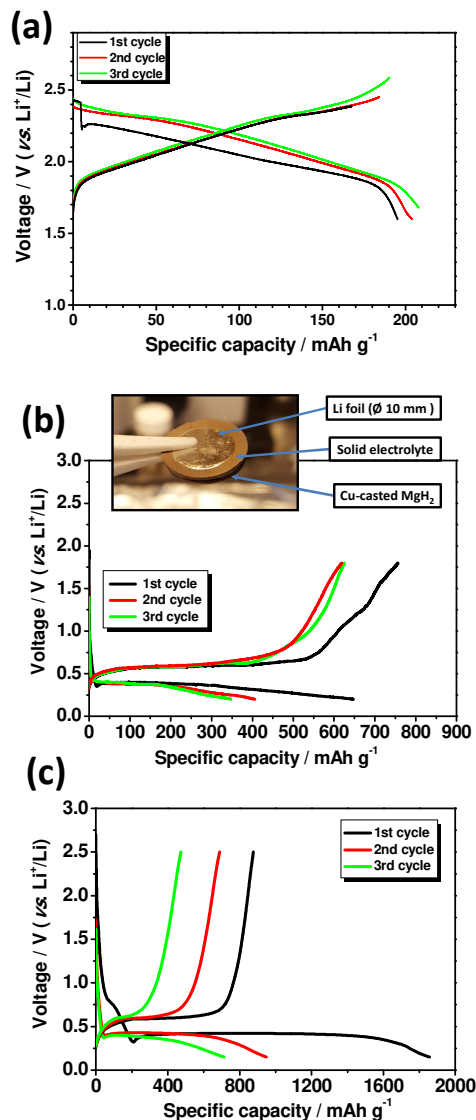

Figure 4. *RT* discharge-charge (3 first cycles) galvanostatic profiles of the (a) standard TiS_2 electrode and (b) MgH_2 tape using the same SE. Inset: picture of the assembled different solid-state layers before being sealed in a battery-cell (30°C, 0.01 mA cm^{-2}). (c) Galvanostatic cycling profiles (3 first cycles) of the same MgH_2 tape using carbonate-based liquid electrolyte for comparison (30°C, 0.25 mA cm^{-2}).

3.2.2   Post-mortem analysis of the electrode/electrolyte interface

The cycled battery in Fig. 4b was analyzed by FIB-SEM. Before cycling, SEM image (Fig.5a) shows the electrode/electrolyte interface where additives (binder and C_{SP}) can be seen (gray regions) in the electrode part. Some of the holes /cracks in the solid electrolyte could be formed by electron beam damage. Fig. 5b shows the cross section secondary electron image at the electrode/electrolyte interface. It displays an overview image of supposed electrode-side surface. Dark areas are Mg-rich, while light areas are P- and S-rich phases (Fig. 5c). Besides, it can be seen various morphological aspects with some porosity in both electrolyte and electrode composite regions. A segregation line seems to be formed and possibly is the origin behind the drop of the voltage after several cycles. Hence, an improvement at the electrode/electrolyte level, i.e. mechanical properties and fabrication process, appears required along an optimization of the electrolyte composition. However, after cycling EDS maps confirm in finer detail the existence of Mg-rich phase solely in the electrode region surrounded by the SE matrix $Li(BH_4)_{0.75}I_{0.25}$–$0.8Li_2S \cdot 0.2P_2S_5$. While the other elements agree roughly with the starting composition and localization, possible migration of B from the SE to the composite electrode can be noticed (Fig. 5c).
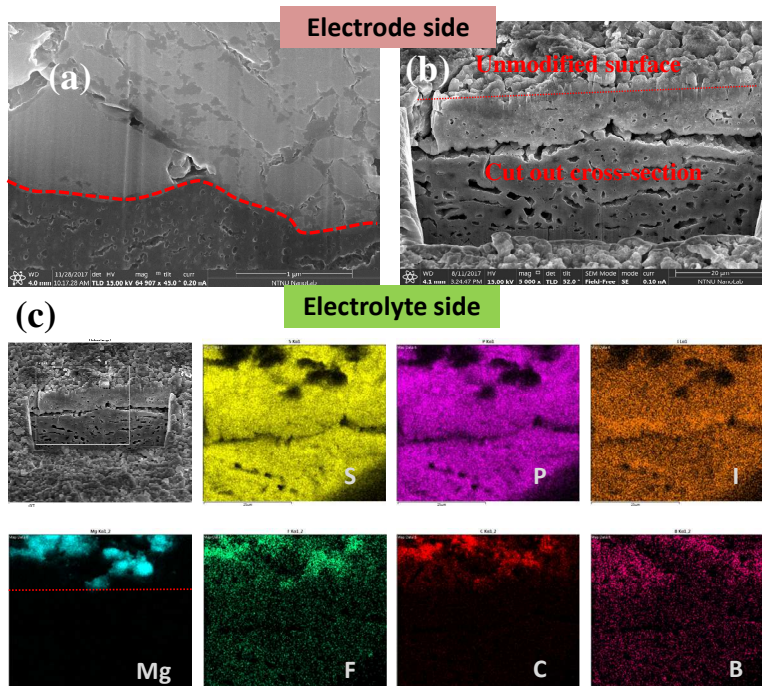
Figure 5. Cross section of the electrode/electrolyte interface (a) before and (b) after cycling obtained by FIB-SEM. Copper foil is removed before microscopic analysis for the battery: MgH_2-tape/SE/Li. (c) Electron micrograph of the electrode/electrolyte interface (top left image) and the corresponding Z^2-scaled contrast maps obtained from simultaneously acquired EDS, where iodine is seen at the same locations as P and S. Carbon (and minor amounts of F of the binder) is observed together with Mg. From the maps chemical composition by at.%, the S:P ratio is higher than 5:2 as expected owing to the presence of Li_2S in addition to P_2S_5.

The different morphological issues that can be encountered in the present configuration are sketched in Fig. 6. In this structural model, it is suggested re-distribution of the MgH_2 particles, likely constituted from nanosized clusters [1,15], into a larger delimited SE volume after cycling. Phases diffusion in the SE part is also expected to compensate the increase of the stress in the material during discharge. The use of SE may play a key role to maintain the mechanical stability of the

electrode composite and prevent pulverization of the highly dispersive LiH [3]. Such

nanoconfinement of the LiH/Mg by-products leads to major enhancement during (de)lithiation by

ensuring local H^- exchanges and short-range Li^+ diffusion pathways along the compatible

borohydride-based electrolyte. Moreover, an interesting feature can be emphasized regarding the

reversibility of this anode, being observed for the 3 cycles. The totality of the discharge capacity is

recovered after re-charge, with slightly higher coulombic efficiency, in which the composite

electrode is following a bulk-volume shrinking (relaxation). This cycling feature can be influenced

by the structural and resistive differences, as well as the existence of path-dependence, between the

lithiated and delithiated states [4]. The absence of additional plateaus during discharge/charge

disproves the existence of any side reaction. Owing to differences in SE composition and treatment,

the interaction of Mg particles with $LiBH_4$ as SE in the 1-2 V range leading to the formation of

$Mg(BH_4)_2$ as described by Zeng *et al.*[10] can not be ascertained, despite the EDS map observation
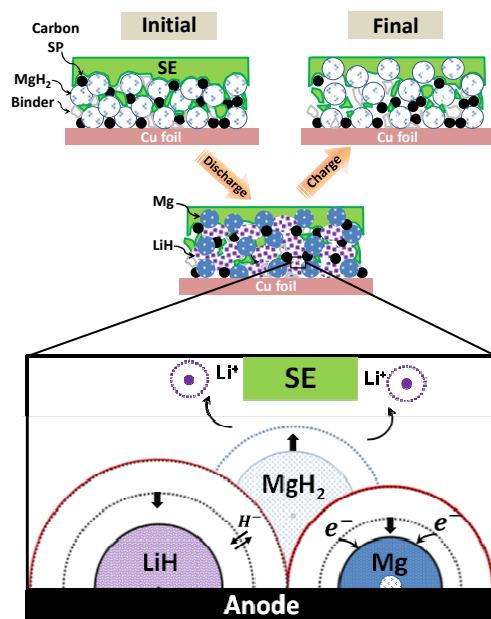
regarding boron.

Figure 6. Sketch of phase transformation and likely interfacial issues during the discharge/charge of solid-state battery MgH$_2$-tape/SE/Li.

4   Conclusion

In summary, this study demonstrates that the conversion-type reactions for an MgH$_2$ anode are dependent on the electrolyte state. The electrochemical cycling experiments show that the loss of the contact between the different electrochemically active phases can be avoided by constructing compacted layers of the electrode-SE composite on a dendritic Cu current collector. So far a major challenge for MgH$_2$ based anodes in Li-ion batteries at RT has been the poor reversibility; however, the current work shows a possible route of improvement via solid state electrolytes. Work is in progress to get more understanding about the interfaces and further optimization based on long term-cycling and rate-capability tests along with the suitable electrolyte.

Acknowledgements

References

[1] Y. Oumellal, A. Rougier, G.A. Nazri, J.M. Tarascon, L. Aymard, Nat. Mater. **7** (2008) 916.

[2] Y. Oumellal, A. Rougier, J.M. Tarascon, L. Aymard, J. Power Sources **192** (2009) 698.

[3] S. Brutti, G. Mulas, E. Piciollo, S. Panero, P. Reale, J. Mater. Chem. **22** (2012) 14531.

[4] D. Meggiolaro, G. Gigli, A. Paolone, P. Reale, M.L. Doublet, S. Brutti, J. Phys. Chem. C **119** (2015) 17044.

[5] P. Poizot, S. Laruelle, S. Grugeon, L. Dupont, J.M. Tarascon, Nature **407** (2000) 496.

[6] L. Aymard, Y. Oumellal, J.-P. Bonnet, Beilstein J. Nanotechnol. **6** (2015) 1821.

[7] S. Ikeda, T. Ichikawa, K. Kawahito, K. Hirabayashi, H. Miyaoka, Y. Kojima, Chem. Commun. **49** (2013) 7174.

[8] S. Ikeda, T. Ichikawa, S. Yamaguchi, H. Miyaoka, Y. Kojima, J. Jpn. Inst. Energy **93** (2014) 926.

[9] S. Ikeda, T. Ichikawa, K. Goshome, S. Yamaguchi, H. Miyaoka, Y. Kojima, J. Solid State Electrochem. **19** (2015) 3639.

[10] L. Zeng, K. Kawahito, S. Ikeda, T. Ichikawa, H. Miyaoka, Y. Kojima, Chem. Commun. **51** (2015) 9773.

[11] L. Zeng, T. Ichikawa, K. Kawahito, H. Miyaoka, Y. Kojima, ACS Appl. Mater. Inter. **9** (2017) 2261.

[12] P. López-Aranguren, N. Berti, A.H. Dao, J. Zhang, F. Cuevas, M. Latroche, C. Jordy, J. Power Sources **357** (2017) 56.

[13] K. Yoshida, S. Suzuki, J. Kawaji, A. Unemoto, S. Orimo, Solid State Ionics **285** (2016) 96.

[14] W. Zaïdi, Y. Oumellal, J.P. Bonnet, J. Zhang, F. Cuevas, M. Latroche, J.L. Bobet, L. Aymard, J. Power Sources **196** (2011) 2854.

[15] Y. Oumellal, C. Zlotea, S. Bastide, C. Cachet-Vivier, E. Leonel, S. Sengmany, E. Leroy, L. Aymard, J.-P. Bonnet, M. Latroche, Nanoscale **6** (2014) 14459.

[16] A. El kharbachi, H.F. Andersen, M.H. Sørby, P.E. Vullum, J.P. Mæhlen, B.C. Hauback, Int. J. Hydrogen Energy **42** (2017) 22551.

[17] K. Takahashi, K. Hattori, T. Yamazaki, K. Takada, M. Matsuo, S. Orimo, H. Maekawa, H. Takamura, J. Power Sources **226** (2013) 61.

[18] R. Miyazaki, T. Karahashi, N. Kumatani, Y. Noda, M. Ando, H. Takamura, M. Matsuo, S. Orimo, H. Maekawa, Solid State Ionics **192** (2011) 143.

[19] A. Hayashi, S. Hama, H. Morimoto, M. Tatsumisago, T. Minami, J. Am. Ceram. Soc. **84** (2001) 477.

[20] A. Unemoto, K. Yoshida, T. Ikeshoji, S.-i. Orimo, Mater. Trans. **57** (2016) 1639.

[21] V. Dyadkin, P. Pattison, V. Dmitriev, D. Chernyshov, J. Synchrotron Rad. **23** (2016) 825.

[22] R.A. Varin, T. Czujko, Z. Wronski, Nanotechnology **17** (2006) 3856.

[23]   R. Schulz, J. Huot, G. Liang, S. Boily, G. Lalande, M.C. Denis, J.P. Dodelet, Mat. Sci. Eng. **267** (1999) 240.

[24]   A. Yamauchi, A. Sakuda, A. Hayashi, M. Tatsumisago, J. Power Sources **244** (2013) 707.

[25]   A. Unemoto, H. Wu, T.J. Udovic, M. Matsuo, T. Ikeshoji, S.-i. Orimo, Chem. Commun. **52** (2016) 564.

[26]   A. Unemoto, T. Ikeshoji, S. Yasaku, M. Matsuo, V. Stavila, T.J. Udovic, S.-i. Orimo, Chem. Mater. **27** (2015) 5407.

[27]   A. Unemoto, M. Matsuo, S.-i. Orimo, Adv. Funct. Mater. **24** (2014) 2267.

[28]   J.E. Trevey, C.R. Stoldt, S.-H. Lee, J. Electrochem. Soc. **158** (2011) A1282.